AGU PUBLICATIONS

JGR

Journal of Geophysical Research: Space Physics

RESEARCH ARTICLE

10.1002/2016JA023011

Key Points:
- Solar wind Poynting flux and electric field saturate at bow shock crossing
- Magnetopause Poynting flux correlates linearly with directly driven electrojets in the ionosphere
- Polar cap saturation is associated with magnetosheath processes

Correspondence to:
T. I. Pulkkinen,
tuija.pulkkinen@aalto.fi

Citation:
Pulkkinen, T. I., A. P. Dimmock, A. Lakka, A. Osmane, E. Kilpua, M. Myllys, E. I. Tanskanen, and A. Viljanen (2016), Magnetosheath control of solar wind–magnetosphere coupling efficiency, *J. Geophys. Res. Space Physics*, *121*, 8728–8739, doi:10.1002/2016JA023011.

Received 29 MAY 2016
Accepted 6 SEP 2016
Accepted article online 14 SEP 2016
Published online 28 SEP 2016

Magnetosheath control of solar wind-magnetosphere coupling efficiency

T. I. Pulkkinen[1], A. P. Dimmock[1], A. Lakka[1], A. Osmane[1], E. Kilpua[2], M. Myllys[2], E. I. Tanskanen[1,3], and A. Viljanen[3]

[1]Department of Radio Science and Engineering, Aalto University School of Electrical Engineering, Aalto, Finland, [2]Department of Physics, University of Helsinki, Helsinki, Finland, [3]Finnish Meteorological Institute, Helsinki, Finland

Abstract We examine the role of the magnetosheath in solar wind-magnetosphere-ionosphere coupling using the Time History of Events and Macroscale Interactions during Substorms plasma and magnetic field observations in the magnetosheath together with OMNI solar wind data and auroral electrojet recordings from the International Monitor for Auroral Geomagnetic Effects (IMAGE) magnetometer chain. We demonstrate that the electric field and Poynting flux reaching the magnetopause are not linear functions of the electric field and Poynting flux observed in the solar wind: the electric field and Poynting flux at the magnetopause during higher driving conditions are lower than those predicted from a linear function. We also show that the Poynting flux normal to the magnetopause is linearly correlated with the directly driven part of the auroral electrojets in the ionosphere. This indicates that the energy entering the magnetosphere in the form of the Poynting flux is directly responsible for driving the electrojets. Furthermore, we argue that the polar cap potential saturation discussed in the literature is associated with the way solar wind plasma gets processed during the bow shock crossing and motion within the magnetosheath.

1. Introduction

Geomagnetic activity in the ionosphere and magnetosphere is driven by energy extracted from the solar wind. This energy is largely transferred through magnetic reconnection process [*Dungey*, 1961], which allows electromagnetic energy in the form of Poynting flux to enter the magnetosphere through the magnetopause boundary [*Palmroth et al.*, 2003]. In addition, a smaller and less variable portion of the energy enters through a variety of viscous processes [*Axford and Hines*, 1961], of which Kelvin-Helmholtz instability at the boundary [*Nykyri and Otto*, 2001; *Kavosi and Rader*, 2015] or kinetic Alfvén waves [*Johnson and Cheng*, 1997] are most dominant.

In light of the above, the key parameters controlling the energy input into the magnetosphere at the magnetopause are the electric field ($\mathbf{E} = -\mathbf{V} \times \mathbf{B}$) component parallel to the magnetopause governing the reconnection rate [*Vasyliunas*, 1975] and the Poynting flux ($\mathbf{S} = \mathbf{E} \times \mathbf{B}/\mu_0$) component normal to the magnetopause [*Rosenqvist et al.*, 2008; *Anekallu et al.*, 2011] that accounts for most of the energy entry. However, due to lack of continuous measurements in the magnetosheath and the difficulty of obtaining sufficient spatial coverage along the magnetopause, most solar wind-magnetosphere-ionosphere coupling studies resort to using the solar wind measurements upstream of the bow shock as the driving parameters.

In the ionosphere, the response is most often characterized by magnetic observations giving an indication of the intensity of the westward and eastward large-scale electrojets [*Kauristie et al.*, 1996] or the polar cap potential [*Troshichev et al.*, 1988]. While the eastward electrojet responds mostly to direct solar wind driving changing the Region 1 currents flowing to and from the ionosphere, the westward electrojet contains an additional component driven by substorm current wedge currents coupling to the nightside magnetotail [*Baker et al.*, 1996]. Thus, the eastward electrojet is a measure of the response to the solar wind variations, while the westward electrojet gives an indication of the level of magnetotail activity. The most widely used proxy of the polar cap potential is the northern polar cap index derived from the Thule magnetometer recordings, while more direct measurements of the polar cap potential can be made by ionospheric radars [*Milan*, 2004] or by low-altitude satellites [*Ahn et al.*, 1992]. In this paper we use the International Monitor for Auroral

Geomagnetic Effects (IMAGE) magnetometer chain observations, which cover latitudes from subauroral to the polar cap, thus giving a comprehensive view of the electrojet intensity in a limited local time sector.

In principle, the solar wind electric field creates a potential difference between dawn and dusk flanks that maps through the open field lines to the polar cap. However, the relationship between the driving solar wind electric field and the ionospheric cross polar potential is not linear throughout the range of driving conditions [e.g., *Reiff et al.*, 1981]. In particular, several studies have demonstrated that for higher solar wind electric field, the polar cap potential is lower than expected based on a linear function. Different studies have produced varying limit values for the saturation electric field [*Ridley*, 2005], which has led to several proposals for the saturation mechanism [*Siscoe et al.*, 2004; *Borovsky et al.*, 2009]. Especially, the Alfvén Mach number has been demonstrated to play a role in the saturation process [*Lavraud and Borovsky*, 2008; *Lopez et al.*, 2010; *Wilder et al.*, 2011; *Myllys et al.*, 2016]. For terminology, we note that the term "polar cap saturation" does not necessarily indicate saturation in an engineering sense (a strict limiting value above which the response remains constant) but a decreased response of the ionospheric cross polar potential to the solar wind electric field.

Pulkkinen et al. [2007] note another type of nonlinearity in the solar wind-magnetosphere coupling: They show that for the same value of the driving electric field ($E_Y = -VB_Z$), a magnetic field-solar wind speed combination in which the speed is higher produces a stronger response in the ionosphere. *Pulkkinen et al.* [2007] point out that this might be caused by differences in the ways the plasma parameters change as the solar wind crosses the bow shock. This idea is supported by the wealth of magnetosheath observations from the Time History of Events and Macroscale Interactions during Substorms (THEMIS) mission demonstrating the complex relationship between the solar wind plasma upstream of the bow shock and the magnetosheath plasma conditions [*Dimmock et al.*, 2014].

In this paper, we examine the role of the magnetosheath in the coupling process using solar wind measurements, THEMIS magnetosheath observations, and IMAGE magnetometer chain data from the auroral zone. Section 2 describes the data and used methodology, section 3 presents the solar wind-magnetosheath correlation, while section 4 focuses on coupling to the ionosphere. Section 5 concludes with discussion.

2. Data and Methods

We use data from the five-spacecraft THEMIS mission [*Angelopoulos*, 2008] from the period 2008–2015 (http://themis.ssl.berkeley.edu/index.shtml). Magnetic field measurements are provided by the fluxgate magnetometer instrument [*Auster and Glassmeier*, 2008], whereas the plasma velocity, density, and pressure measurements come from the THEMIS on board moments from the electrostatic analyzer instrument [*McFadden et al.*, 2008]. We use data from all five satellites during the minimum between solar cycles 23 and 24 and the rising and maximum phases of solar cycle 24.

In order to analyze the magnetosheath statistical properties as a function of upstream solar wind conditions, we examine the THEMIS observations in the magnetosheath interplanetary medium (MIPM) reference frame [*Verigin et al.*, 2006]. In this frame the $\hat{e}_x$ axis is oriented antiparallel to the upstream solar wind flow and the $\hat{e}_y$ axis is perpendicular to the $\hat{e}_x$ axis with the interplanetary magnetic field (IMF) vector in the $\hat{e}_x$-$\hat{e}_y$ plane. Thus, each point is rotated around the Sun-Earth line to the plane of the IMF, reducing the three-dimensional data set to a two-dimensional plane. In this representation, the quasi-parallel shock is always on the "dawn" side, while the quasi-perpendicular shock is on the "dusk" side. The radial fractional distance is measured from 0 at the magnetopause to 1 at the bow shock. The bow shock position is calculated from the model by *Verigin et al.* [2001] and the magnetopause position from the model by *Shue et al.* [1998]. This coordinate system organizes the THEMIS observations in relation to position relative to magnetopause and bow shock locations as well as the IMF Parker spiral orientation [*Dimmock and Nykyri*, 2013].

Figure 1a shows the magnetosheath electric field component parallel to the magnetopause $E_{\|,\mathrm{MS}}(= -\mathbf{V}_{\mathrm{MS}} \times \mathbf{B}_{\mathrm{MS}})_{\|}$ in the magnetosheath. The parallel component was computed by taking the component tangent to the model magnetopause at the location of the observation and shows the value of the electric field (in mV/m). For reference, typical solar wind values produce electric fields of a few mV/m (e.g., $B_Z = -5$ nT and $V_X = -400$ km/s $\rightarrow E_Y = 2$ mV/m). Figure 1b shows the electric field values near the magnetopause obtained by computing the average value close to the magnetopause (here defined to be within 20% of the magnetosheath thickness) as a function of the angle from noon direction (positive toward afternoon local times). Note that due to the MIPM frame used, the magnetopause and shock locations show the average locations over the observed period,

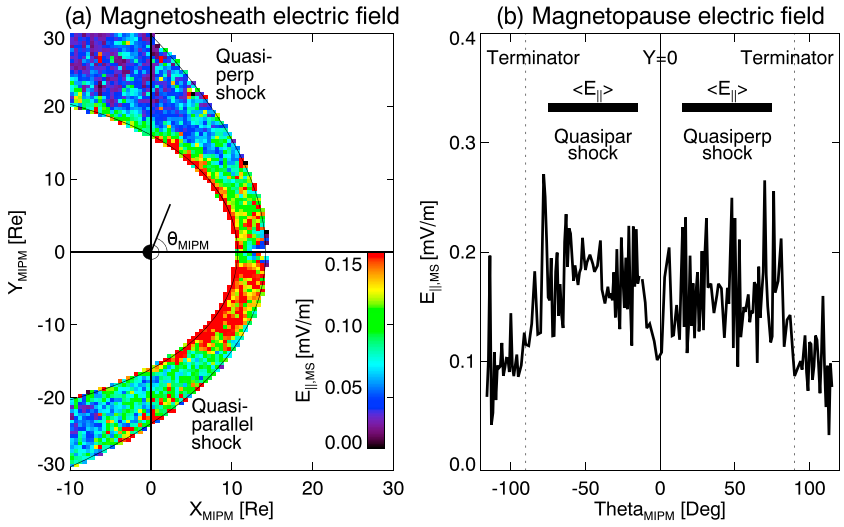

Figure 1. (a) Magnetosheath electric field parallel to the model magnetopause ($E_{||,MS}$) from THEMIS observations in the MIPM frame (color coded). (b) Parallel electric field near the magnetopause as function of angle from noon (positive toward afternoon local times).

and each measurement is shown in a bin that places it in the correct position with respect to distance to the bow shock and magnetopause.

The IMAGE magnetometer network consists of about 30 magnetometer stations maintained by 10 institutes from Estonia, Finland, Germany, Norway, Poland, Russia, and Sweden (http://space.fmi.fi/image/). The stations cover geographic latitudes from 58° to 79° geographic latitude (from Tartu in Estonia to Ny Ålesund in Svalbard) and between 10° and 30° Eastern longitude. The IMAGE magnetometer network records variations in the geomagnetic field at 10 s cadence [*Tanskanen*, 2009].

Amm [1997] and *Amm and Viljanen* [1999] developed a method for expressing the ground magnetic field variations in terms of ionospheric currents. Using this methodology and the IMAGE magnetometer chain observations, we compute the latitudinal profile of the equivalent current density in the auroral zone. The baseline is subtracted by selecting manually a quiet time period for each day. The total current in the westward and eastward electrojets flowing through the network longitude is calculated by integration of the current profile over the above mentioned range of latitudes. The equivalent currents are based on the total horizontal variation field on the ground, so the effect of telluric currents is not subtracted. However, their contribution to the total variation during substorms is typically around 20%, which does not cause a significant bias [*Tanskanen et al.*, 2001]. Furthermore, the local *IU* and *IL* indices are computed in a way analogous to the auroral electrojet upper and lower (*AU*, *AL*) indices at 1 min temporal resolution [*Tanskanen et al.*, 2002].

While these indices can be computed for all local times, the interpretation of the measurements to represent the global eastward and westward electrojet intensity maxima requires the chain to be in an adequate local time position. The *IL* index has been shown to correlate well with the global *AL* index in the local time sector 2000–0400 MLT, which corresponds to roughly 1800–0200 UT [*Kauristie et al.*, 1996]. Within that time range, due to the latitudinal coverage of the network, the *IL* index gives a better indication of the substorm intensity. Similarly, the eastward electrojet response to the *IU* index is clearly visible when the network is in the dusk sector, roughly 1600–2000 UT. In the following, we limit the analysis of the midnight sector westward electrojet using the westward electrojet values during 2000–2400 UT (about 2200–0200 h local time) and eastward electrojet values during 1600–2000 UT (about 1800–2200 h local time) to ensure that the IMAGE chain is accurately capturing the maximum auroral electrojet activity.

Figure 2a shows a sample of IMAGE magnetometer data in keogram format. The *X* component of the magnetic field at each of the 31 stations on 5 April 2014 at 1200–2400 UT is shown color coded. Figure 2b shows the total eastward and westward electrojet current through the central longitude of the chain (21.1° Eastern longitude).

The solar wind driver properties upstream of the bow shock are examined using the OMNI data set compiled at National Space Science Data Center (http://spdf.gsfc.nasa.gov/). The data set provides the solar wind

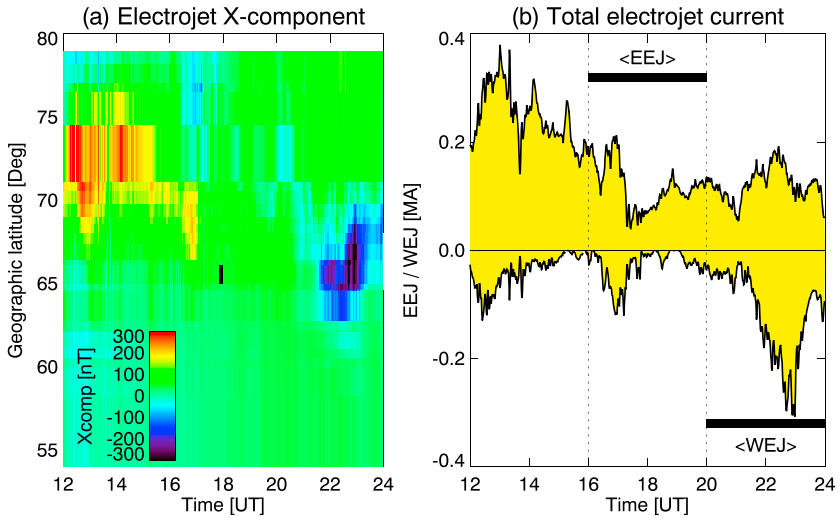

Figure 2. (a) Magnetic field *X* component from the IMAGE magnetometer chain on 5 April 2014, 1200–2400 UT (color coded). (b) Eastward (EEJ) and westward (WEJ) electrojet total current through the central longitude of the chain for the same time period.

plasma density and velocity, the interplanetary magnetic field, and other parameters recorded by a variety of spacecraft. Time delays from the satellite position to the subsolar magnetopause are accounted for by appropriate propagation of the observations (see *King* [2005] for data processing and propagation methods).

3. Magnetosheath Saturation

The orbital coverage of the THEMIS mission is such that it takes 12 months to gather sufficient data to produce a map such as shown in Figure 1a. We produce partially overlapping maps of 12 month averages, which allow us to look at the long-term evolution of the magnetosheath properties at 3 month cadence. Averages of the magnetic field (B), velocity (V), density (N), electric field (E), Poynting flux ($\mathbf{S} = \mathbf{E} \times \mathbf{B}/\mu_0$ where μ_0 is vacuum permeability), and plasma $\beta(=2p\mu_0/B^2$ where p is the plasma pressure) are evaluated at the magnetopause for each interval by taking an average between $-75^\circ < \theta_{\mathrm{MIPM}} < -15^\circ$ and $15^\circ < \theta_{\mathrm{MIPM}} < 75^\circ$ to avoid the region near local noon and near the terminators, where the uneven data coverage produces large scatter to the averages. In this way, the magnetosheath plasma observations for any given period are reduced to a single number representing the magnetopause average. Figure 3b shows the plasma parameters from THEMIS in the magnetosheath averaged in the way discussed above during 2008–2015. Figure 3a show the corresponding solar wind and interplanetary magnetic field parameters processed in an analogous way for the same time period. While it is clear that overall the magnetopause values follow quite well the solar wind variations in this averaged sense, in the following we examine in more detail the correlations between the parameters.

Figure 4 shows the correlation of the solar wind values with the magnetopause averages using data in Figure 3. The data points marked with gray show periods when the solar wind electric field average exceeds 1.8 mV/m, picking the stronger driving periods mainly toward the end of our study period (i.e., during solar maximum conditions). It is clear that for low level of driving, there is a good linear correlation between solar wind and magnetopause values. However, for the more active periods, the magnetopause values seem to saturate such that higher solar wind driver values no longer produce higher driving at the magnetopause. While the saturation effect is not clearly visible in the speed or magnetic field correlations, it is very notable when looking at the parameters controlling the energy input into the magnetosphere, namely, the electric field parallel to the boundary and the Poynting flux normal to the magnetopause.

In order to examine whether the magnetosheath saturation discussed above is reflected in the ionospheric measurements, we examine the long-term correlations of the IMAGE measurements with the solar wind and magnetosheath averages. Figure 5 shows correlations of the solar wind and magnetopause driving parameters (electric field and Poynting flux) with the ionospheric response (westward and eastward electrojets). The IMAGE magnetometer measurements are averaged to 3 month averages for winter (December–February), spring (March–May), summer (June–August), and fall (September–November) using only the time periods

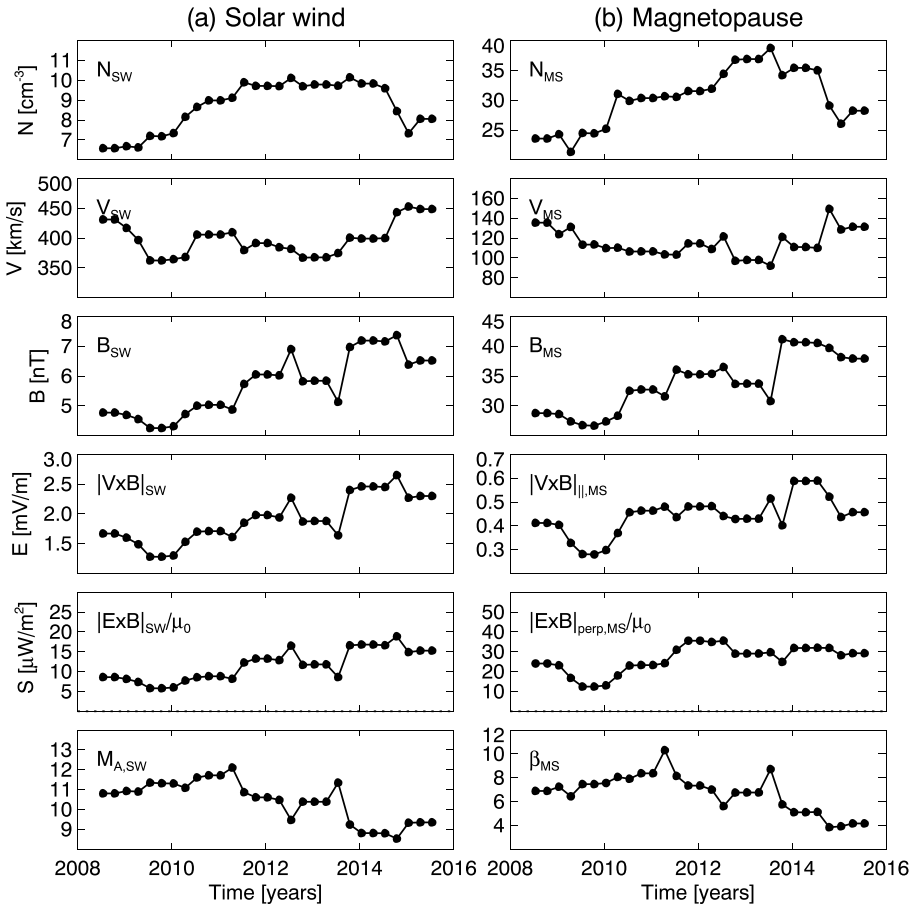

Figure 3. The 12 month sliding averages at 3 month cadence of solar wind and magnetopause plasma parameters. (a) Solar wind density (*N*), speed (*V*), magnetic field (*B*), electric field (*E*), Poynting flux (*S*), and Alfvén Mach number (*MA*). (b) Magnetopause density, speed, magnetic field, electric field parallel to the magnetopause, Poynting flux normal to the magnetopause, and plasma β (for computation of the averages see text).

16–20 UT for the eastward electrojet and 20–24 UT for the westward electrojet. Similarly to Figure 4, the points with solar wind electric field exceeding 1.8 mV/m are shown gray. In all cases, the correlation coefficients are higher for the magnetopause — ionosphere correlation than for the corresponding solar wind — ionosphere correlation. This is true for all solar wind parameters (not shown). Especially, the westward electrojet correlations show the saturation in the solar wind-ionosphere correlations, which is removed when examining the magnetopause driver correlation with the ionospheric response.

4. Seasonal Variability in the Ionosphere

The IMAGE magnetometer measurements contain strong seasonal variability [*Pulkkinen et al.*, 2011]. We therefore examine each season separately, looking at the winter (December–February), spring (March–May), summer (June–August), and fall (September–November) values as 3 month averages. In this way, it is possible to distinguish characteristic annual variations as well as seasonal variations around equinox and solstice conditions. Figure 6 shows the 3 month averages of the electrojet values (using only the time periods 16–20 UT for the eastward electrojet and 20–24 UT for the westward electrojet) with seasons color coded and the sunspot number indicating the solar activity shown gray in the background (not to scale). The eastward electrojet values show a clear annual variability on top of a slower solar cycle variation with higher summer values caused by the increased luminosity and ionization in the ionosphere. The westward electrojet variations are more complex, exhibiting responses to the varying geomagnetic activity conditions as well as the semiannual variability with higher fall and spring values associated with the Russell-McPherron effect [*Russell and McPherron*, 1973]. The maximum disturbances in electrojets occur during the declining phase of the solar cycle.

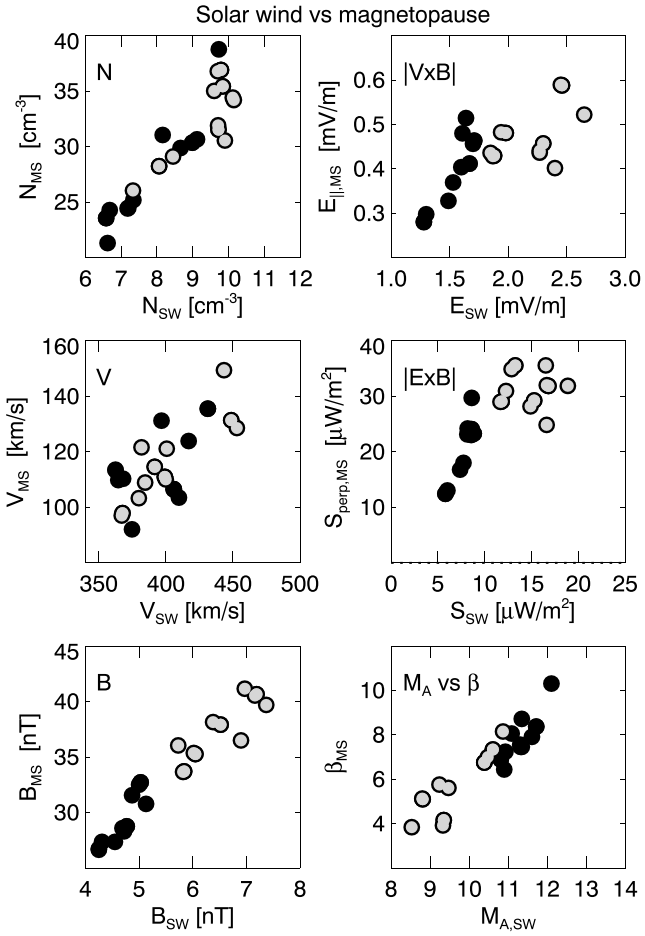

Figure 4. Solar wind versus magnetopause plasma parameters. (left column) Density (*N*), speed (*V*), and magnetic field (*B*). (right column) Solar wind electric field (*E*) and Poynting flux (*S*); the magnetosheath electric field and Poynting flux values are components parallel and normal to the boundary, respectively. Alfvén Mach number (*MA*) versus magnetopause plasma β. Points with driving solar wind electric field $E_{SW} \geq 1.8$ mV/m are shown in gray.

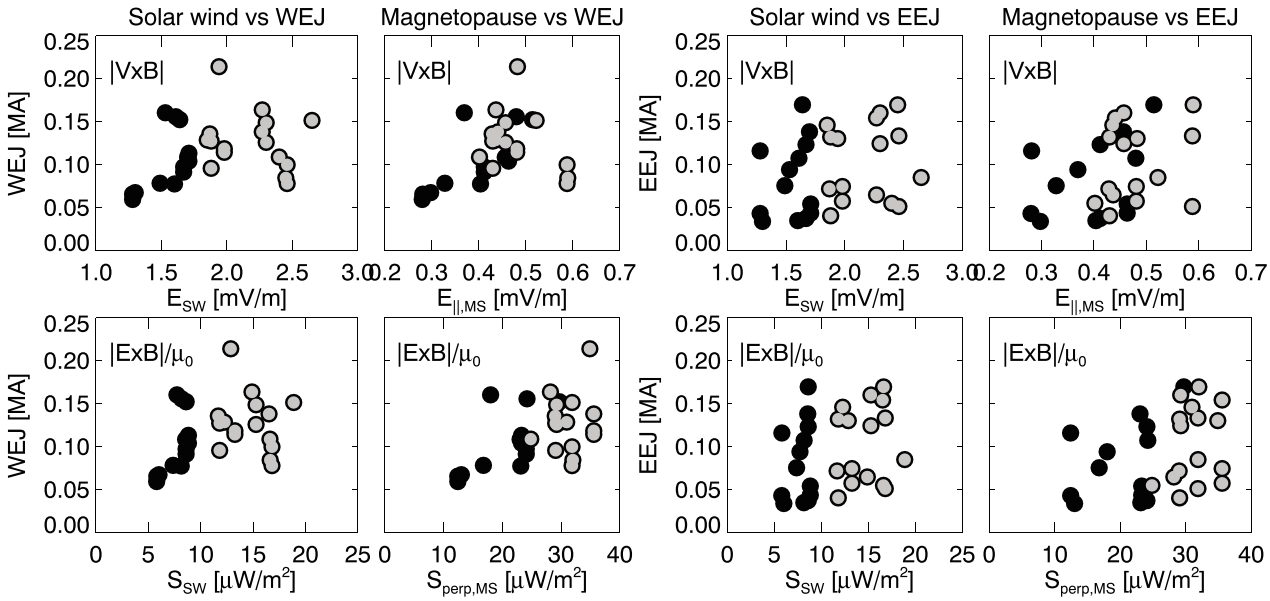

Figure 5. Westward electrojet current (20–24 UT) and eastward electrojet current (16–20 UT) averages as function of solar wind and magnetopause electric field (*E*) and Poynting flux (*S*). Points with driving solar wind electric field $E_{SW} \geq 1.8$ mV/m are shown in gray.

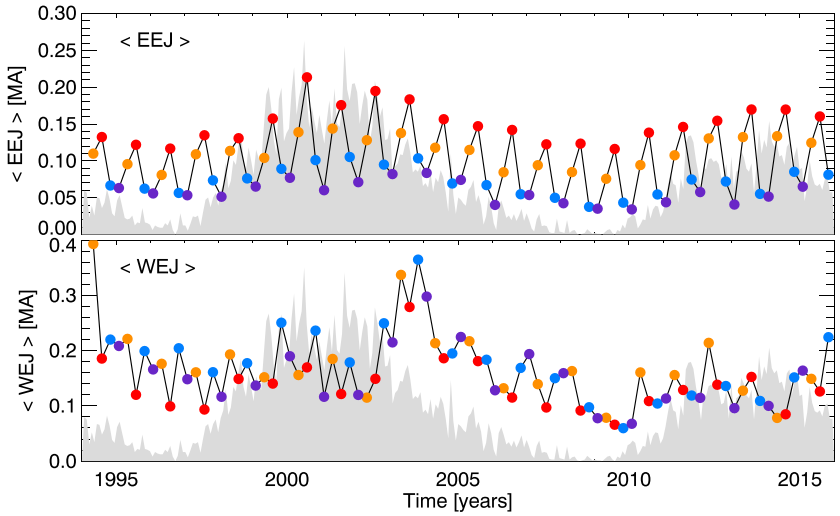

Figure 6. Eastward electrojet current (16–20 UT) and westward electrojet current (20–24 UT) averaged to 3 month averages centered around equinoxes and solstices. Winter values are shown in dark blue, summer values in red, fall values with bright blue, and spring values in orange. The sunspot number (not to scale) is shown with the gray shading.

The scatter especially in the eastward electrojet case in Figure 5 is partially due to the significant seasonal variability evident in Figure 6. Figure 7 shows the correlations similar to Figure 5 but with the seasons color coded with the same colors as in Figure 6 with bright and dark blue denoting fall and winter values and orange and red denoting spring and summer values. The figure clearly shows that the winter values are best organized and show a good linear correlation with the Poynting flux for both eastward and westward electrojets. The spring and summer values show much more scatter, which partially is associated with the fact that as discussed above, the overall activity in the electrojets is stronger at these times and hence also the variability is larger. However, part of the scatter may also originate from the baseline method, which does not remove the regular diurnal variation caused by ionospheric ionization due to solar radiation. The strong annual variability is responsible for almost all the scatter in the eastward electrojet-magnetopause Poynting flux correlation.

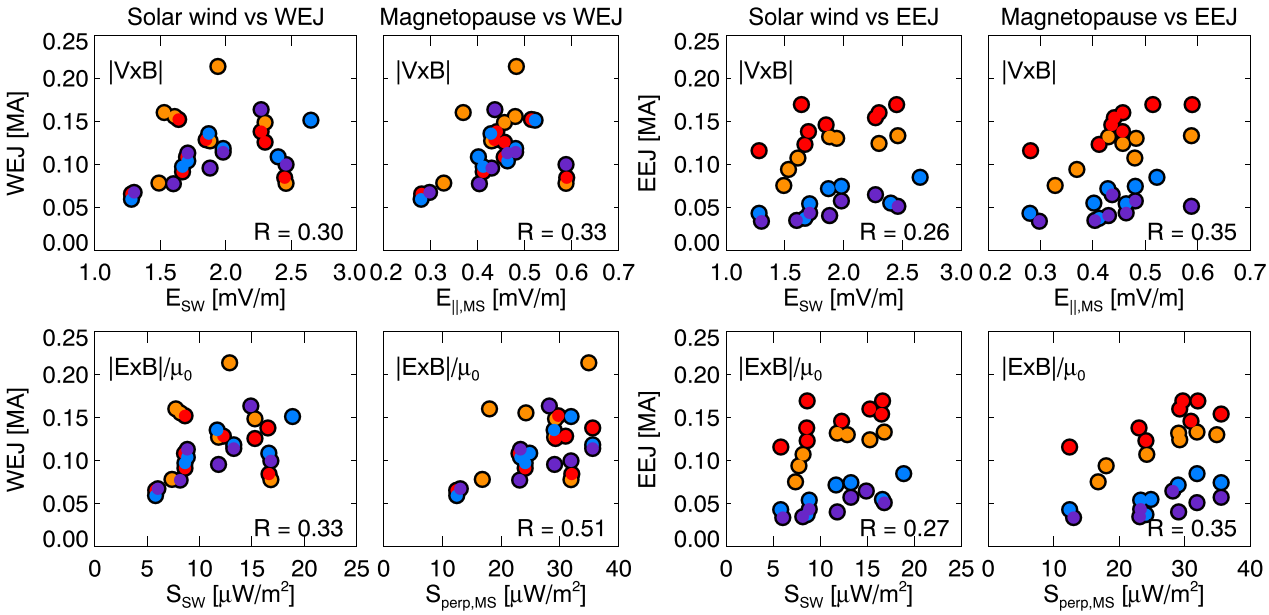

Figure 7. Westward electrojet current (20–24 UT) and eastward electrojet current (16–20 UT) averages as function of solar wind and magnetosheath electric field (*E*) and Poynting flux (*S*). Winter values are shown in dark blue, summer values in red, fall values with bright blue, and spring values in orange.

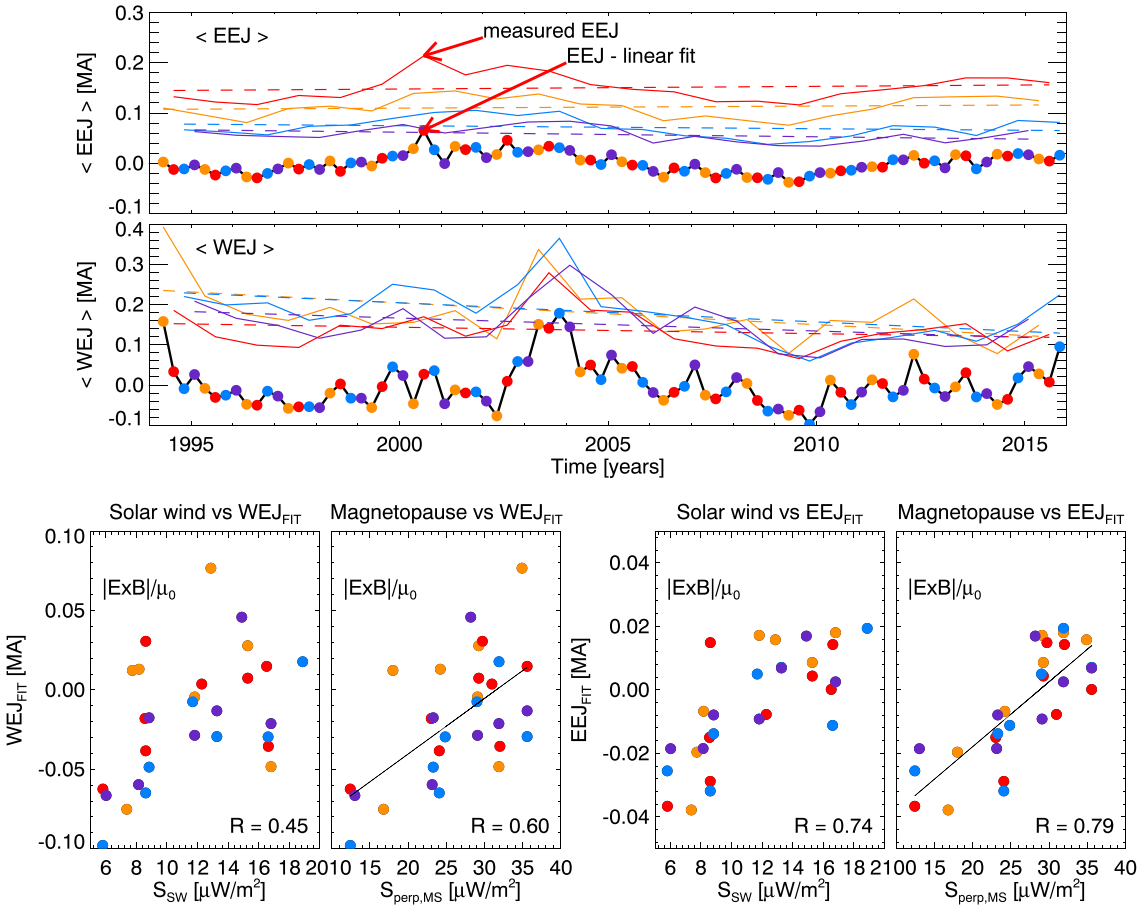

Figure 8. (top) Eastward electrojet current (16–20 UT) and westward electrojet current (20–24 UT) averaged to 3 month averages centered around equinoxes and solstices. Winter values are shown in dark blue, summer values in red, fall values with bright blue, and spring values in orange thin lines. The filled circles indicate a best fit of the form $y_{\mathrm{fit},s} = a_s + b_s y_s$ for all seasons s using the winter values as baseline. (bottom) Westward electrojet current (20–24 UT) and eastward electrojet current (16–20 UT) averages as function of solar wind and magnetosheath Poynting flux (S). The seasons are color coded as above. The correlation coefficients are shown at the bottom right corner, and a best fit linear fit is indicated for the magnetopause–ionosphere comparisons.

In order to remove the scatter caused by the annual and/or seasonal variations arising, e.g., from the ionospheric illumination conditions, we examine each season as independent time series. Figure 8 (top) shows the original seasonal values as solid thin lines. The dashed lines of the same color show a linear fit to the data (see Table 1). The filled circles with thick solid line below shows the difference of the measured value and the linear fit ($\mathrm{EEJ}_s - \mathrm{linfit}(\mathrm{EEJ}_s)$; $\mathrm{WEJ}_s - \mathrm{linfit}(\mathrm{WEJ}_s)$ for all seasons s), combining all seasons to the same data series. It is clear that for the eastward electrojet, the annual variability can be largely removed by this method. On the other hand, the semiannual and other driver-dependent variability in the westward electrojet is not removed by this procedure.

Figure 8 (bottom) show the correlations of the electrojet current with linear trends removed (data with filled circles in Figure 8, top) with the Poynting flux in the solar wind and the Poynting flux incident at the magnetopause. Comparison of the correlation coefficients with those in Figure 7 shows that subtracting the

Table 1. Linear Trends Removed From Seasonal Values in Figure 8 ($EJ_{\mathrm{fit},s} = a_s + b_s(\mathrm{Time}_s(\mathrm{years}) - 1994)$ for All Seasons s) for Both Eastward Electrojet (EEJ) and Westward Electrojet (WEJ)

Season	$a_{s,\mathrm{EEJ}}$	$b_{s,\mathrm{EEJ}}$	$a_{s,\mathrm{WEJ}}$	$b_{s,\mathrm{WEJ}}$
Spring	0.11	0.00041	0.24	−0.0054
Summer	0.14	0.00053	0.15	−0.0016
Fall	0.08	−0.00061	0.23	−0.0048
Winter	0.07	−0.00092	0.19	−0.0032

linear trends produces a significant improvement for the eastward electrojet, while the scatter in the westard electrojet remains large and the correlation coefficients remain quite low. However, both eastward and westard electrojet intensity saturates at higher Poynting flux values when the Poynting flux is calculated using upstream solar wind values. Such saturation is absent when Poynting flux is estimated using magnetosheath values incident at the magnetopause. Figure 7 (right) showing the correlation between the eastward electrojet and the magnetopause Poynting flux quite clearly indicates a close linear relationship between the electromagnetic energy input through the magnetopause with the electrojet activity in the ionosphere.

5. Discussion

In this paper, we demonstrate that the energy input from the magnetosheath through the magnetopause into the magnetosphere is not linearly dependent on the energy incident in the solar wind upstream of the bow shock. Our results show that energy access to the vicinity of the magnetopause is reduced when the driving solar wind electric field and Poynting flux increase, leading to a situation where higher solar wind driving does not produce equally higher energy input into the magnetosphere. Again, we emphasize that these results cannot be used to prove the existence of a fixed "saturation value" that would be a strict upper limit on the energy entry to the magnetopause. On the other hand, we show that the Poynting flux at the magnetopause is linearly correlated with the directly driven auroral electrojets. The conclusion from these results is that the polar cap saturation is associated with processes in the magnetosheath and at the bow shock.

Earlier works have addressed the following mechanisms for the polar cap potential saturation: weakening of the magnetopause reconnection through reducing the merging line length [*Raeder and Lu*, 2005; *Ridley*, 2005; *Kan et al.*, 2010], limited capacity of the ionosphere to feed Region 1 currents [*Siscoe et al.*, 2002a], the decreased magnetic field strength at the dayside magnetopause due to enhanced Region 1 currents [*Hill et al.*, 1976; *Siscoe et al.*, 2002b], or formation of Alfvén wings under low Mach number conditions [e.g., *Ridley*, 2007; *Kivelson and Ridley*, 2008]. Our results indicate saturation of the electric field occurs as the plasma and magnetic field traverse the bow shock and the magnetosheath, which decreases the magnetopause reconnection rate and energy entry to values lower than one would expect based on the upstream solar wind observations. On the other hand, we did not find evidence that the energy entry into the ionosphere would be limited by ionospheric processes, once the energy has gained access into the magnetosphere.

Previous polar cap saturation studies have used the cross polar cap potential to identify saturation events. In this study, the auroral electrojets are used to indicate the ionospheric responses to solar wind and magnetosphere driving, as measurements of the polar cap potential are not available for such large data sets as treated here. While individual events can be obtained from Super Dual Auroral Radar Network, even there the accuracy of the measurements strongly depends on the echo quality and the UT of the observation determining the locations of the radars with respect to the polar cap and auroral electrojets. We have therefore assumed that the polar cap potential determines the strength of the R1 currents, which in turn determine the intensity of the driven electrojets. While over short timescales the polar cap potential and electrojet intensity may have different temporal evolutions, over the longer timescales examined here they are well correlated [*Troshichev et al.*, 1988; *Ahn et al.*, 1992; *Stauning*, 2013]

Recently, *Myllys et al.* [2016] studied solar wind-magnetosphere coupling efficiency during magnetic clouds and the associated turbulent sheath regions and conclude that the polar cap saturation is more prevalent during the cloud proper (low Mach number plasma) than during the sheath (higher Mach number plasma). As the Mach number controls the plasma beta in the magnetosheath, this can be explained by the Mach number dependence on how the solar wind plasma and interplanetary magnetic field transfer across the bow shock: As empirically shown by our results, low solar wind Mach number leads to lower plasma beta at the magnetopause, which allows magnetic forces to accelerate the plasma in a direction perpendicular to the magnetic field, along the magnetopause [*Lavraud and Borovsky*, 2008; *Lopez et al.*, 2010]. Consistent with our results, this would lead to saturation during lower Mach number conditions. Note that due to the long averaging, we cannot determine the instantaneous value of the Mach number at which the response changes—we only record the averaged effects embedding the changes in the response.

While the solar wind-magnetosphere coupling has been extensively studied in the past, any correlation examinations are hampered by nonideal observations that cause large scatter in any data. Ionospheric electrojets are often characterized by auroral electrojet indices, which cover all local times but only a limited range of latitudes thus leading to underestimation of the electrojet current in conditions where the measuring station

is not directly underneath the peak of the current. Latitudinal magnetometer chains such as IMAGE allow not only estimation of the maximum current but also the total current, as under most conditions the chain covers the range of latitudes where the electrojet resides. However, the limitations of such chains include limited local time coverage as well as significant seasonal variations that come from the varying illumination conditions affecting the state of the ionosphere [*Newell et al.*, 2010; *Lyatsky et al.*, 2001]. Here we have limited our study to the local time sectors where the IMAGE chain has a good vantage point to measure the eastward and westward electrojets and has used a simple method of subtracting a linear trend from the data to remove the seasonal effects. This led to substantial improvements in the input-output correlations between the magnetopause energy input and the electrojet total current. Note also that we use midnight sector westward electrojet data from 22 to 02 LT in order to maximally include the effects of the substorm-associated activity, which also responds to increased driving (and hence correlates with Polar Cap index potential). However, use of morning sector westward electrojet (02–06 LT) leads to very similar results (not shown); the morning and midnight electrojets have high correlation with the former having a slightly lower intensity but similar trends over the timescales discussed in this paper [*Pulkkinen et al.*, 2011].

The THEMIS five-spacecraft mission has produced a comprehensive set of observations within the terrestrial magnetosheath covering a significant portion of a solar cycle and all regions of the magnetosheath in a uniform manner. This data set allows us to examine both the spatial and temporal variations in the magnetosheath properties under different solar wind and interplanetary magnetic field driving conditions. Earlier studies have demonstrated the dependence of the dawn-dusk asymmetries on the solar wind driver [*Dimmock et al.*, 2015] and the variations in the magnetosheath conditions under high and low solar wind speed [*Pulkkinen et al.*, 2015]. In this paper, we examine the long-term evolution of the magnetosheath properties and especially focus on values close to the magnetopause, which allows direct association with the energy entry processes. This methodology has allowed us to examine the average dependence of the solar wind parameters with the conditions at the magnetopause and with the electrojet intensity in the ionosphere and thus include a previously missing piece of the chain of processes governing the ionospheric driving.

The solar wind-magnetosphere-ionosphere coupling and energy entry processes into the magnetosphere are key to developing understanding of the harmful effects space weather phenomena can cause to man-made systems in space and on ground. Recent discussion on the topic has dealt with the probability and effects of extreme events—aiming at estimating the maximum disturbances and the damage that might be caused following such events [e.g., *Cliver and Svalgaard*, 2004; *Riley*, 2012; *Baker et al.*, 2013]. From this point of view it would be important to understand the ionospheric response under extreme conditions—whether the response remains linear for all driving values or if their processes would limit the equatorward motion of the electrojet to some minimum latitude. This is left as a future study.

6. Summary

Using THEMIS, OMNI, and IMAGE magnetometer chain data we analyzed that the electric field and Poynting flux in the solar wind and at the magnetopause. While the relationship between the solar wind electric field and Poynting flux to those observed at the magnetopause is close to linear when the driving electric field is relatively low, this is not true for higher values of the electric field. It appears that for large solar wind electric field values, the values reaching the magnetopause are lower than expected from the linear trend. We furthermore show that similar relationship can be shown between the solar wind electric field and the ionospheric electrojets. On the other hand, the relationship between the magnetopause electric field and Poynting flux to the ionospheric electrojets is linear throughout the range of examined values. This indicates that the "saturation" effect takes place in the magnetosheath. We propose that this process is at least partially responsible for the observed polar cap saturation at high solar wind driving conditions.

Acknowledgments
We thank the institutes who maintain the IMAGE Magnetometer Array. Data are available through http://space.fmi.fi/image/. We thank the NASA/GSFC Space Physics Data Facility for maintaining and developing the OMNIWeb and OMNI data. Data are available through http://spdf.gsfc.nasa.gov/. We thank the THEMIS instrument teams for the use of their data. The THEMIS data are available through http://themis.ssl.berkeley.edu/index.shtml. This work has been supported by Academy of Finland grant 1267087.

References

Ahn, B.-H., Y. Kamide, H. W. Kroehl, and D. J. Gorney (1992), Cross-polar cap potential difference, auroral electrojet indices, and solar wind parameters, *J. Geophys. Res.*, *97*(A2), 1345–1352, doi:10.1029/91JA02432.

Amm, O. (1997), Ionospheric elementary current systems in spherical coordinates and their application, *J. Geomagn. Geoelectr.*, *49*, 947–955.

Amm, O., and A. Viljanen (1999), Ionospheric disturbance magnetic field continuation from the ground to the ionosphere using spherical elementary current systems, *Earth, Planets, and Space*, *51*(6), 431–440.

Anekallu, C. R., M. Palmroth, T. I. Pulkkinen, S. Haaland, E. A. Lucek, and I. S. Dandouras (2011), Energy conversion at the Earth's magnetopause using single and multi-spacecraft methods, *J. Geophys. Res.*, *116*, A11204, doi:10.1029/2011JA016783.

Angelopoulos, V. (2008), The THEMIS mission, *Space Sci. Rev.*, *141*(1–4), 5–34.

Auster, H. U., and K. H. Glassmeier (2008), The THEMIS fluxgate magnetometer, *Space Sci. Rev.*, *141*(1–4), 235–264.
Axford, W. I., and C. O. Hines (1961), A unifying theory of high-latitude geophysical phenomena and geomagnetic storms, *Can. J. Phys.*, *39*, 1433–1464.
Baker, D. N., T. I. Pulkkinen, V. Angelopoulos, W. Baumjohann, and R. L. McPherron (1996), The neutral line model of substorms: Past results and present view, *J. Geophys. Res.*, *101*, 12,975–130,10.
Baker, D. N., X. Li, A. Pulkkinen, C. M. Ngwira, M. L. Mays, A. B. Galvin, and K. D. C. Simunac (2013), A major solar eruptive event in July 2012: Defining extreme space weather scenarios, *Space Weather*, *11*(10), 1542–7390, doi:10.1002/swe.20097.
Borovsky, J. E., B. Lavraud, and M. M. Kuznetsova (2009), Polar cap potential saturation, dayside reconnection, and changes to the magnetosphere, *J. Geophys. Res.*, *114*, A3224, doi:10.1029/2009JA014058.
Cliver, E. W., and L. Svalgaard (2004), The 1859 solar–terrestrial disturbance and the current limits of extreme space weather activity, *Sol. Phys.*, *224*(1), 407–422, doi:10.1007/s11207-005-4980-z.
Dimmock, A. P., and K. Nykyri (2013), The statistical mapping of magnetosheath plasma properties based on THEMIS measurements in the magnetosheath interplanetary medium reference frame, *J. Geophys. Res. Space Physics*, *118*, 4963–4976, doi:10.1002/jgra.50465.
Dimmock, A. P., K. Nykyri, and T. I. Pulkkinen (2014), A statistical study of magnetic field fluctuations in the dayside magnetosheath and their dependence on upstream solar wind conditions, *J. Geophys. Res. Space Physics*, *119*, 6231–6248, doi:10.1002/2014JA020009.
Dimmock, A. P., K. Nykyri, H. Karimabadi, A. Osmane, and T. I. Pulkkinen (2015), A statistical study into the spatial distribution and dawn-dusk asymmetry of dayside magnetosheath ion temperatures as a function of upstream solar wind conditions, *J. Geophys. Res. Space Physics*, *120*, 2767–2782, doi:10.1002/2014JA020734.
Dungey, J. (1961), Interplanetary magnetic field and the auroral zones, *Phys. Rev. Lett.*, *6*(2), 47–48.
Hill, T. W., A. J. Dessler, and R. A. Wolf (1976), Mercury and mars: The role of ionospheric conductivity in the acceleration of magnetospheric particles, *Geophys. Res. Lett.*, *3*(8), 429–432.
Johnson, J. R., and C. Z. Cheng (1997), Kinetic Alfvén waves and plasma transport at the magnetopause, *Geophys. Res. Lett.*, *24*, 1423–1426, doi:10.1029/97GL01333.
Kan, J. R., H. Li, C. Wang, B. B. Tang, and Y. Q. Hu (2010), Saturation of polar cap potential: Nonlinearity in quasi-steady solar wind–magnetosphere–ionosphere coupling, *J. Geophys. Res.*, *115*, A08226, doi:10.1029/2009JA014389.
Kauristie, K., T. I. Pulkkinen, R. J. Pellinen, and H. J. Opgenoorth (1996), What can we tell about global auroral-electrojet activity from a single meridional magnetometer chain?, *Ann. Geophys.*, *14*, 1177–1185, doi:10.1007/s00585-996-1177-1.
Kavosi, S., and J. Rader (2015), Ubiquity of Kelvin-Helmholtz waves at Earth's magnetopause, *Nat. Commun.*, *6*, 7019, doi:10.1038/ncomms8019.
King, J. H. (2005), Solar wind spatial scales in and comparisons of hourly Wind and ACE plasma and magnetic field data, *J. Geophys. Res.*, *110*, A02104, doi:10.1029/2004JA010649.
Kivelson, M. G., and A. J. Ridley (2008), Saturation of the polar cap potential: Inference from Alfvén wing arguments, *J. Geophys. Res.*, *113*, A05214, doi:10.1029/2007JA012302.
Lavraud, B., and J. E. Borovsky (2008), Altered solar wind-magnetosphere interaction at low Mach numbers: Coronal mass ejections, *J. Geophys. Res.*, *113*, A00B08, doi:10.1029/2008JA013192.
Lopez, R. E., R. Bruntz, E. J. Mitchell, M. Wiltberger, J. G. Lyon, and V. G. Merkin (2010), Role of magnetosheath force balance in regulating the dayside reconnection potential, *J. Geophys. Res.*, *115*, A12216, doi:10.1029/2009JA014597.
Lyatsky, W., P. T. Newell, and A. Hamza (2001), Solar illumination as cause of the equinoctial preference for geomagnetic activity, *Geophys. Res. Lett.*, *28*(12), 2353–2356.
McFadden, J. P., C. W. Carlson, D. Larson, M. Ludlam, R. Abiad, B. Elliott, P. Turin, M. Marckwordt, and V. Angelopoulos (2008), The THEMIS ESA plasma instrument and in-flight calibration, *Space Sci. Rev.*, *141*(1–4), 277–302.
Milan, S. E. (2004), Dayside and nightside contributions to the cross polar cap potential: Placing an upper limit on a viscous-like interaction, *Ann. Geophys.*, *22*, 3771–3777, doi:1432-0576/ag/2004-22-3771.
Myllys, M., E. Kilpua, B. Lavraud, and T. I. Pulkkinen (2016), Solar wind–magnetosphere coupling efficiency during ejecta and sheath region driven geomagnetic storms, *J. Geophys. Res. Space Physics*, *121*, 4378–4396, doi:10.1002/2016JA022407.
Newell, P. T., T. Sotirelis, and S. Wing (2010), Seasonal variations in diffuse, monoenergetic, and broadband aurora, *J. Geophys. Res.*, *115*, A03216, doi:10.1029/2009JA014805.
Nykyri, K., and A. Otto (2001), Plasma transport at the magnetospheric boundary due to reconnection in Kelvin-Helmholtz vortices, *Geophys. Res. Lett.*, *28*(18), 3565–3568, doi:10.1029/2001GL013239.
Palmroth, M., T. I. Pulkkinen, P. Janhunen, and C.-C. Wu (2003), Stormtime energy transfer in global MHD simulation, *J. Geophys. Res.*, *108*(A1), 1048, doi:10.1029/2002JA009446.
Pulkkinen, T. I., C. C. Goodrich, and J. G. Lyon (2007), Solar wind electric field driving of magnetospheric activity: Is it velocity or magnetic field?, *Geophys. Res. Lett.*, *34*, L21101, doi:10.1029/2007GL031011.
Pulkkinen, T. I., E. I. Tanskanen, A. Viljanen, N. Partamies, and K. Kauristie (2011), Auroral electrojets during deep solar minimum at the end of solar cycle 23, *J. Geophys. Res.*, *116*, A04207, doi:10.1029/2010JA016098.
Pulkkinen, T. I., A. Dimmock, A. Osmane, and K. Nykyri (2015), Solar wind energy input to the magnetosheath and at the magnetopause, *Geophys. Res. Lett.*, *42*, 4723–4730, doi:10.1002/2015GL064226.
Raeder, J., and G. Lu (2005), Polar cap potential saturation during large geomagnetic storms, *Adv. Space Res.*, *36*(10), 1804–1808.
Reiff, P. H., R. W. Spiro, and T. W. Hill (1981), Dependence of polar cap potential drop on interplanetary parameters, *J. Geophys. Res.*, *86*(A9), 7639–7648.
Ridley, A. J. (2005), A new formulation for the ionospheric cross polar cap potential including saturation effects, *Ann. Geophys.*, *23*(11), 3533–3547.
Ridley, A. J. (2007), Alfvn wings at Earth's magnetosphere under strong interplanetary magnetic fields, *Ann. Geophys.*, *25*(2), 533–542.
Riley, P. (2012), On the probability of occurrence of extreme space weather events, *Space Weather*, *10*(2), 1542–7390, doi:10.1029/2011SW000734.
Rosenqvist, L., A. Vaivads, A. Retino, T. Phan, H. J. Opgenoorth, I. Dandouras, and S. Buchert (2008), Modulated reconnection rate and energy conversion at the magnetopause under steady IMF conditions, *Geophys. Res. Lett.*, *35*, L08104, doi:10.1029/2007GL032868.
Russell, C. T., and R. L. McPherron (1973), Semiannual variation of geomagnetic activity, *J. Geophys. Res.*, *78*, 92–108.
Shue, J.-H., J. K. Chao, H. C. Fu, C. T. Russell, P. Song, K. K. Khurana, and H. J. Singer (1998), Magnetopause location under extreme solar wind conditions, *J. Geophys. Res.*, *103*, 17,691–17,700, doi:10.1029/98JA01103.
Siscoe, G., J. Raeder, and A. J. Ridley (2004), Transpolar potential saturation models compared, *J. Geophys. Res.*, *109*, A09203, doi:10.1029/2003JA010318.

Siscoe, G. L., N. U. Crooker, and K. D. Siebert (2002a), Transpolar potential saturation: Roles of region 1 current system and solar wind ram pressure, *J. Geophys. Res.*, *107*(A10), 1321, doi:10.1029/2001JA009176.

Siscoe, G. L., G. M. Erickson, B. U. O. Sonnerup, N. C. Maynard, J. A. Schoendorf, K. D. Siebert, D. R. Weimer, W. W. White, and G. R. Wilson (2002b), Hill model of transpolar potential saturation: Comparisons with MHD simulations, *J. Geophys. Res.*, *107*, A61075, doi:10.1029/2001JA000109.

Stauning, P. (2013), The polar cap index: A critical review of methods and a new approach, *J. Geophys. Res. Space Physics*, *118*, 5021–5038, doi:10.1002/jgra.50462.

Tanskanen, E., A. T. Viljanen, T. I. Pulkkinen, R. J. Pirjola, L. Häkkinen, A. Pulkkinen, and O. Amm (2001), At substorm onset, 40% of AL comes from underground, *J. Geophys. Res.*, *106*(A7), 13,119–13,134.

Tanskanen, E., T. I. Pulkkinen, H. E. J. Koskinen, and J. A. Slavin (2002), Substorm energy budget during low and high solar activity: 1997 and 1999 compared, *J. Geophys. Res.*, *107*, 1086, doi:10.1029/2001JA900153.

Tanskanen, E. I. (2009), A comprehensive high-throughput analysis of substorms observed by IMAGE magnetometer network: Years 1993–2003 examined, *J. Geophys. Res.*, *114*, A05204, doi:10.1029/2008JA013682.

Troshichev, O. A., V. G. Andrezen, S. Vennerstroem, and E. Friis-Christensen (1988), Magnetic activity in the polar cap: A new index, *Planet. Space Sci.*, *36*, 1095–1102.

Vasyliunas, V. (1975), Theoretical models of magnetic field line merging, *Rev. Geophys.*, *13*(1), 303–336, doi:10.1029/RG013i001p00303.

Verigin, M. I., G. A. Kotova, J. Slavin, A. Szabo, M. Kessel, J. Safrankova, Z. Nemecek, T. I. Gombosi, and K. Kabin (2001), Analysis of the 3-D shape of the terrestrial bow shock by Interball/Magion 4 observations, *Adv. Space Res.*, *28*(6), 857–862, doi:10.1016/S0273-1177(01)00502-6.

Verigin, M. I., M. Tatrallyay, G. Erdos, and G. A. Kotova (2006), Magnetosheath interplanetary medium reference frame: Application for a statistical study of mirror type waves in the terrestrial plasma environment, *Adv. Space Res.*, *37*, 515–521, doi:10.1016/j.asr.2005.03.042.

Wilder, F. D., C. R. Clauer, J. B. H. Baker, E. P. Cousins, and M. R. Hairston (2011), The nonlinear response of the polar cap potential under southward IMF: A statistical view, *J. Geophys. Res.*, *116*, A12229, doi:10.1029/2011JA016924.